Are Mixed-Halide Ruddlesden-Popper Perovskites Really Mixed?

Stefano Toso[1,2,3,], Irina Gushchina[1], Allen G. Oliver[1], Liberato Manna[3], Masaru Kuno[1,4]*

1 Department of Chemistry and Biochemistry, University of Notre Dame, Notre Dame, IN 46556, USA
2 International Doctoral Program in Science, Università Cattolica del Sacro Cuore, 25121 Brescia, Italy
3 Department of Nanochemistry, Istituto Italiano di Tecnologia, Via Morego 30, 16163 Genova, Italy
4 Department of Physics, University of Notre Dame, Notre Dame, IN 46556, USA

E-mail: stefano.toso@iit.it

TOC

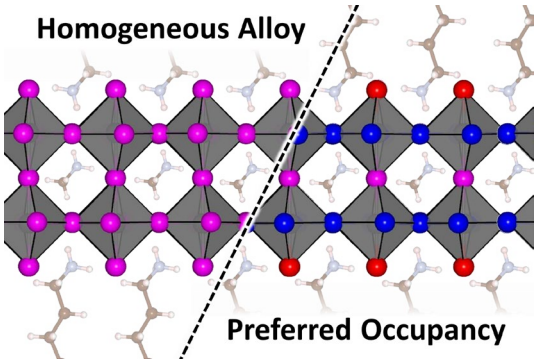

ABSTRACT

Mixing bromine and iodine within lead halide perovskites is a common strategy to tune their optical properties. This comes at the cost of instability, as illumination induces halide segregation and degrades device performances. Hence, understanding the behavior of mixed-halide perovskites is crucial for applications. In 3D-perovskites like $MAPb(Br_xI_{1-x})_3$ (MA=methylammonium), all halide crystallographic sites are similar, and the consensus is that bromine and iodine are homogeneously distributed prior to illumination. By analogy, it is often assumed that Ruddlesden-Popper layered perovskites like $(BA)_2MAPb_2(Br_xI_{1-x})_7$ (BA=butylammonium) behave alike. However, these materials possess a much wider variety of halide sites featuring diverse coordination environments, that might be preferentially occupied by either bromine or iodine. This leaves an open question: are mixed-halide Ruddlesden-Popper perovskites really mixed? By combining powder and single-crystal diffraction experiments, we demonstrate that this is not the case: bromine and iodine in RP perovskites preferentially occupy different sites, regardless of the crystallization speed.

MAIN TEXT

Ruddlesden-Popper (RP) lead-halide perovskites are a class of two-dimensional (2D) semiconductors that have recently gained relevance as promising candidates for optoelectronic and photovoltaic applications.[1–6] Described by the formula $L_2A_{n-1}Pb_nX_{3n+1}$,[7] they consist of n bidimensional layers of corner-sharing $[PbX_6]^{4-}$ octahedra (X = Cl, Br, I) held together by isotropic cations (A = Cs^+, methylammonium [MA], formamidinium [FA], …). Individual layers, in turn, are separated by long-chain ammonium cations such as butylammonium [L = BA] or phenylethyl ammonium [L = PEA].[3]

A demand for band gap tuning, electronic structure engineering, and integration into three-dimensional (3D)-perovskite solar cells is now extending interest to mixed bromide-iodide RP perovskites, $L_2A_{n-1}Pb_n(Br_xI_{1-x})_{3n+1}$, where x indicates the bromine fraction. Recent reports confirm that mixing halides in RP perovskites offers additional control over their optical properties[8] and enables the use of a wider variety of L cations than single-halide RP perovskites.[9] Other studies have demonstrated the creation of vertical and horizontal heterojunctions, obtained by stacking pre-made RP sheets[10] or by exploiting halide-diffusion reactions.[11]

Despite progress in the area, applications of 2D mixed-halide perovskites are limited by photoinduced anion segregation. Recent investigations into their photostability highlight a tendency of halide anions to migrate within crystals under illumination,[12–14] similar to what is observed in 3D mixed-halide $APb(Br_xI_{1-x})_3$ perovskites.[12,13] In this regard, photoinduced anion segregation appears to be an intrinsic instability of lead halide perovskites as a whole.

As early studies shed light on the behavior of mixed-halide RP perovskites under external stimuli, questions have arisen about their properties when at rest. Indeed, while the structures of 3D mixed-halide perovskites are well described as halide alloys,[15,16] there are reasons to believe that the situation is more complex in 2D mixed-halide RP perovskites. Compared to 3D-perovskites, RP structures offer a greater diversity of halide crystallographic sites. Of these, some sites are embedded deep

within inorganic layers (central sites, Ct), while others protrude directly into the organic cation layers (apical sites, Ap), or alternatively create extended horizontal networks that form the inorganic layers (equatorial sites, Eq).

This diversity of coordination environments may therefore promote the occupation of certain sites by different anions, by virtue of differences in ionic radii or interaction affinities with cations. Recently published theoretical predictions bring arguments to support such preferential positioning of halides in $(PEA)_2Pb(Br_xI_{1-x})_4$.[8] These results are corroborated by single-crystal X-ray diffraction studies on $(ter\text{-}BA)_2Pb(Br_{0.5}I_{0.5})_4$.[9] The same effect has also been reported for other layered metal halides such as $(MA)_2Cu(Cl_xBr_{1-x})_4$.[17–19] This poses a question: are lead-based mixed-halide RP perovskites really mixed alloys?

To answer this question, we investigate the structure of bilayer $(BA)_2MAPb_2(Br_xI_{1-x})_7$ RP perovskites. We have chosen bilayers (n = 2) because they offer a wider variety of halide crystallographic sites compared to n = 1 monolayers, where sites embedded deep in the inorganic layers (Ct) are missing due to insufficient thickness. Samples have been synthesized by adapting published methods[7,10] with details provided in the Supporting Information (**SI**). Briefly, for each sample a stock solution is prepared by dissolving methylammonium, butylammonium, and lead iodides and bromides in a hot mixture of concentrated HI, HBr and H_3PO_2. Precursor ratios, detailed in **Table S1,** determine the resulting sample stoichiometry. Once solubilized, solutions are cooled to 35-40 °C, causing the precipitation of RP perovskite powders that are used for powder X-ray diffraction (PXRD) analyses. Alternatively, RP crystals are grown on substrates by drop casting the warm solution. This initiates nucleation and growth, which is then halted by drying substrates with a paper tissue. The procedure yields platelet-shaped crystals with lateral sizes of ~10-100 μm (**Figure 1a**), which are used for compositional analysis and optical microscopy. Their habit is remindful of the RP structure,[7] having wide and flat [010] facets, laterally terminated by perpendicular [101] and $[10\bar{1}]$ facets.

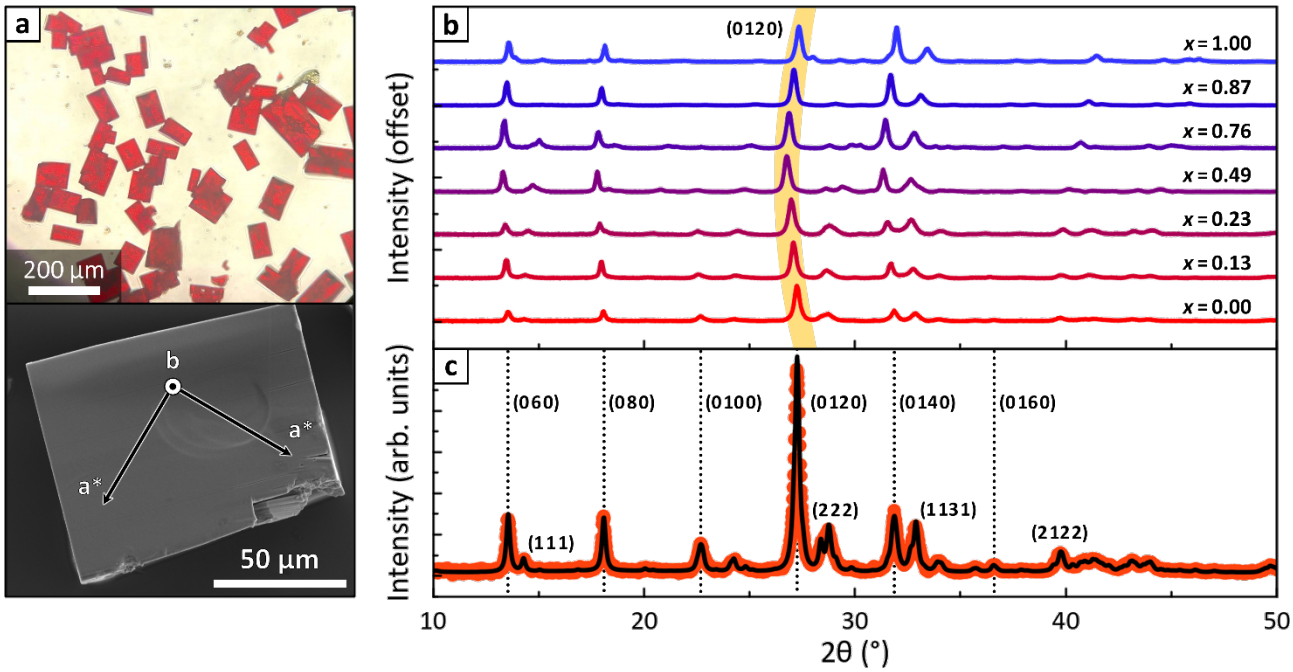

Figure 1. PXRD characterization of $(BA)_2MAPb_2(Br_xI_{1-x})_7$. a) Top: optical microscopy image of $(BA)_2MAPb_2(Br_xI_{1-x})_7$ crystals. Bottom: SEM image of a representative crystal, with overlaid lattice vectors. b) PXRD patterns of $(BA)_2MAPb_2(Br_xI_{1-x})_7$ samples. Highlighted are the (0120) peaks, whose shift toward lower angles highlights the anomalous unit cell expansion along the *b* cell axis for mixed-halide compositions. c) Le Bail profile fit of the $(BA)_2MAPb_2I_7$ PXRD pattern. Vertical dotted grey lines indicate the family of (02*k*0) peaks typical of RP perovskites. Some (*hkh*) peaks, which ensure a reliable determination of the *a** parameter, have also been indexed.

Samples compositions have been verified using Scanning Electron Microscopy – Energy Dispersive X-ray Spectroscopy (SEM-EDXS). All mixed-halide specimens were found to be significantly richer in iodine than expected from their stock solution feed ratios. This indicates a tendency of RP structures to incorporate iodine over bromine. A calibration curve, relating measured experimental compositions to those of starting precursor solutions, was therefore constructed (See **SI**, **Figure S1**). In what follows, samples compositions are labeled using x_{tot} = Br/[Br+I] where Br and I are the measured halide atomic fractions: x_{tot} = 0 stands for pure-iodide samples, while x_{tot} = 1 stands for pure-bromide samples.

All samples were characterized via PXRD (**Figure 1b**). Their diffraction patterns feature a series of intense and periodic (02*k*0) peaks, typical of RP perovskites (see also **SI, Figure S2**).[6,7] A Le Bail

profile fit was performed on all patterns (**Figure 1c** shows it for $x = 0$, other fits are available in the **SI**, **Figure S3**) to trace how unit cell parameters change with halide composition. Because RP perovskites are pseudo-tetragonal materials, most reflections that differentiate a and c (*i.e.*, $h \neq l$) are weak and overlap strongly. This makes their individual measurements unreliable. In contrast, a pseudo-tetragonal a^* parameter that represents an average of a and c is easily determined, based on strong and well-resolved (hkh) reflections.

As expected, a^* decreases linearly from $a^* = 8.92$ Å for $x = 0$ to $a^* = 8.33$ Å for $x = 1$ (**Figure 2a**). The b parameter, however, does not change linearly with halide composition (**Figure 2b**). Rather, it first rises and then falls, reaching a maximum at $x_{tot} = 0.5$ ($b = 39.9$ Å). This behavior is foreshadowed in **Figure 1b** by the marked shift of (02k0) peaks toward lower angles. Together, a^* and b result in a monotonic decrease of the unit cell volume ($V_{cell} = a^{*2}b$) as x_{tot} increases from 0 to 1 (**Figure 2c**). Only a mild positive inflection is seen due to the nonlinear behavior of b.

Such anomalous dependence of b on the halide composition suggests that lead-based mixed-halide RP perovskites *do not* behave as ideal alloys when it comes to placing I^- and Br^- in the structure. To rationalize this behavior, we therefore construct a geometric model (**Figure 2**) that relates RP unit cell parameters to the distribution of halide anions in different crystallographic sites (Ap, Ct, and Eq). The model is semiquantitative and rationalizes the observed PXRD structural trends summarized in **Figures 2a-c**.

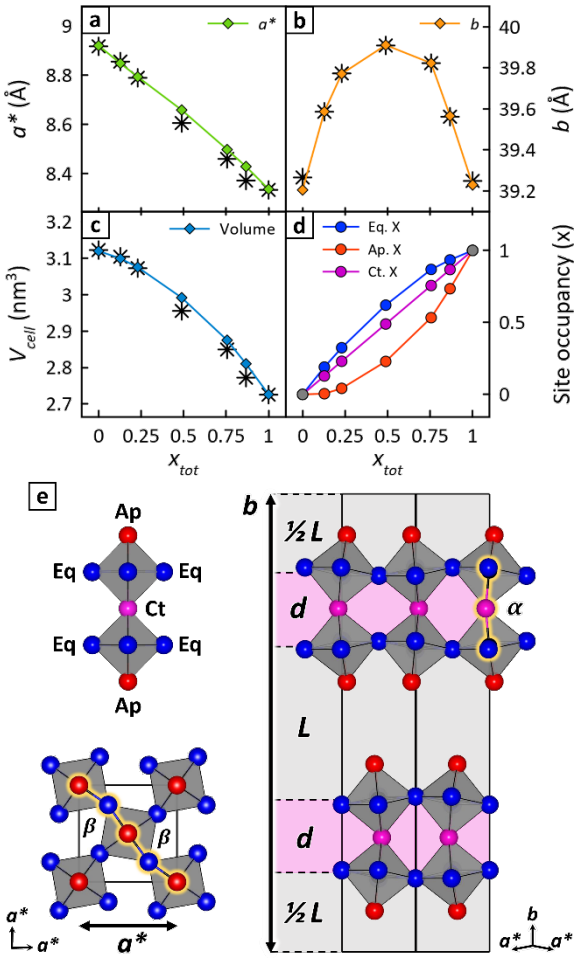

Figure 2. Impact of halide distribution on $(BA)_2MAPb_2X_7$ unit cell parameters. a-c) Experimental RP unit cell parameters (black asterisks) and model predictions (colored lines). d) Halide distribution in apical (Ap), equatorial (Eq), and central (Ct) sites, corresponding to parameters predicted in panels (a-c). e) Visual representation of the model, showing how a^* and b are functions of bond lengths, tilt angles, and of the organic cation spacing L. The inorganic layer thickness, d, is defined in **Equation 2**. In panels (d) and (e), red, blue, and purple colors identify Ap, Eq, and Ct sites, respectively.

In the model, unit cell parameters a^* and b are functions of [Pb-X] bond lengths, of horizontal and vertical octahedra tilt angles (α and β), and of the organic cation layers thickness L (**Equations 1**,**2)**. All parameters in **Equations 1** and **2** depend on the halide occupation of Ap, Eq, and Ct sites, which are related to each other and to experimentally established sample halide compositions, x_{tot}, via the material stoichiometry (**Equation 3**).

$$a^* = \frac{4 \cdot [\mathrm{Pb-X}]_{\mathrm{Eq}} \cdot \sin\left(\frac{\beta}{2}\right)}{\sqrt{2}} \tag{1}$$

$$b = 2L + 4d = 2L + 4 \cdot [\mathrm{Pb-X}]_{\mathrm{Ct}} \cdot \sin\left(\frac{\alpha}{2}\right) \tag{2}$$

$$x_{\mathrm{tot}} = \frac{4}{7}x_{\mathrm{Eq}} + \frac{2}{7}x_{\mathrm{Ap}} + \frac{1}{7}x_{\mathrm{Ct}}\,. \tag{3}$$

Lead-halide bond lengths ([Pb-X]) are modeled as linear combinations of limiting [Pb-Br] and [Pb-I] bond distances, as measured by Single-Crystal X-ray Diffraction (SCXRD) on $(BA)_2MAPb_2Br_7$ and $(BA)_2MAPb_2I_7$, weighted by the fractional occupation of respective halide sites (**Table S2**). In **Equations 1** and **2**, the subscripts Eq and Ct identify the site involved in each [Pb-X] bond and the bond itself. Similarly, α and β are estimated from limiting values determined by SCXRD (**Table S3**). We additionally note that octahedra tilting modes adopted by pure-bromide and pure-iodide structures are incompatible.[7,20] We therefore assume that a transition structure at $x_{tot} = 0.5$ does not experience octahedra tilt in any direction. This assumption is later proven correct. Finally, L is estimated by assuming that the volume occupied by butylammonium chains remains constant in all structures (see SI and **Table S4** for further discussion). A detailed description of the model and explanations of how [Pb-X], α, β and L depend on the halide composition of Ap, Eq, and Ct sites can be found in the **SI** (**Figure S4**).

The only free variable in the model is x_{Eq}. Indeed, given the similarity to bulk halide sites in 3D-perovskites, Ct sites are assumed to be occupied by I^- and Br^- with no preference (i.e., $x_{Ct} \approx x_{tot}$). Consequently, x_{Ap} is a function of x_{Eq} ($x_{\mathrm{Ap}} = 3x_{\mathrm{tot}} - 2x_{\mathrm{Eq}}$, from **Equation 3**). With this, PXRD-

extracted *b* values (**Figure 2b**) are fit using the model by varying x_{Eq}. The fit simultaneously yields model-predicted a^* and V_{cell} values that can be further compared with experiments (**Figure 2a** and **2c**) to assess the model's overall performance.

Solid colored lines in **Figure 2** reveal that the model captures the linear trend of a^* in **Figure 2a**, the peaked behavior of *b* in **Figure 2b**, and the mild positive inflection of V_{cell} in **Figure 2c** as x_{tot} increases from 0 to 1. These results correspond to a marked excess of iodine in unit cell apical positions and bromine in equatorial positions. The trend is observed over the entire $(BA)_2MAPb_2(Br_xI_{1-x})_7$ composition range (**Figure 2d**). As a point of reference, for $x_{tot} = 0.5$ the halide distribution predicted by the model is: Ap = 23% Br, Eq = 62% Br, and Ct = 50% Br.

Overall, these results demonstrate that the anisotropic unit cell expansion observed by PXRD arises from a preferential positioning of halide anions. Such an expansion is rationalized as the combination of two effects. First, the prevalence of larger I^- ions in apical positions results in an elongation of [Pb-X] bonds parallel to the unit cell *b*-axis. Second, the prevalence of smaller Br^- ions in equatorial positions shrinks the lattice on the *a*-*c* plane. This laterally compresses the BA cations and forces them to expand along the *b*-axis. What results is an increase of the interlayer distance, *L*. This conclusion is corroborated by SCXRD-solved structures of $(BA)_2MAPb_2Br_7$ and $(BA)_2MAPb_2I_7$, where $L = 13.49$ Å in the former and $L = 13.15$ Å in the latter. As both effects are solely dependent on [Pb-X] bond distances, the behavior is expected to be general across RP structures made using different organic cations.

Furthermore, the anisotropic expansion along *b*, measured as a bowing in the position of PXRD (02*k*0) reflections, appears to be a reliable approach for detecting the preferential positioning of halide anions in mixed-halide RP structures. Indeed, further simulations (**Figure S5**) indicate that the *b* parameter could grow as much as +4.3% if halides displayed full preferentiality for Apical and Equatorial sites, and would instead decrease by -1.3% if halides were randomly alloyed (with reference value being the average *b* parameter for pure-halide structures, 39.26 Å).

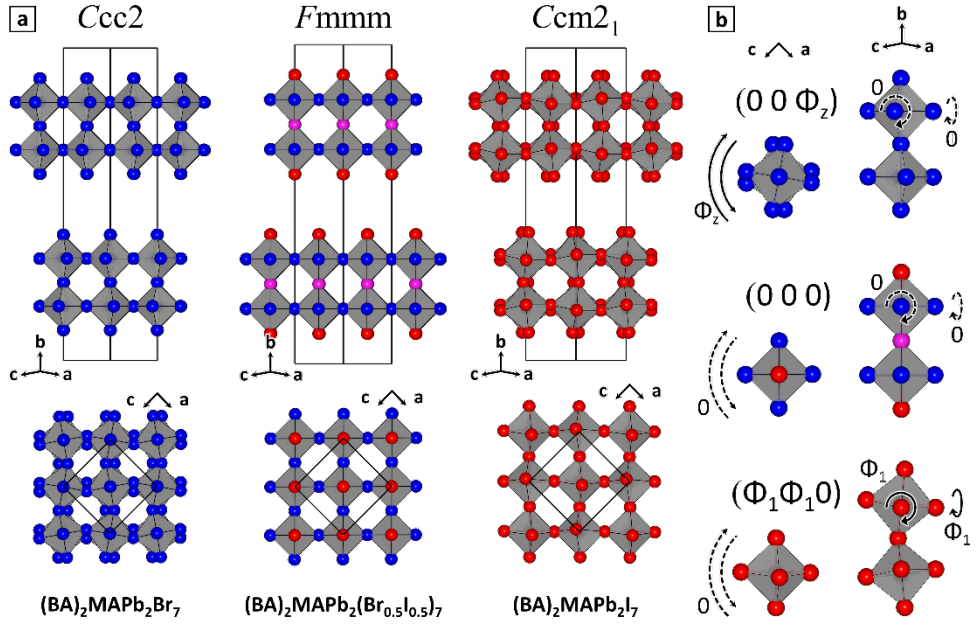

Figure 3. Structures of pure- and mixed-halide $(BA)_2MAPb_2X_7$ samples. a) Crystal structures of $(BA)_2MAPb_2Br_7$ [left], $(BA)_2MAPb_2(Br_{0.5}I_{0.5})_7$ [middle], and $(BA)_2MAPb_2I_7$ [right] as solved by SCXRD. Top: (101) projection. Bottom: (010) projection. Halide site color code: blue = Br (exclusive or prevalent); red = I (exclusive or prevalent), purple = comparable Br and I fractions. Organic cations have been omitted for clarity. b) Representation of octahedra tilting modes in structures, as described by Aleksandrov notation.[21]

To support and validate our model, single-crystal specimens of $(BA)_2MAPb_2I_7$, $(BA)_2MAPb_2Br_7$, and mixed-halide $x_{tot} = 0.5$ $(BA)_2MAPb_2(Br_{0.5}I_{0.5})_7$ were grown by slowly cooling precursor solutions and were subsequently analyzed by SCXRD. Data have been collected at room temperature to ensure that structure parameters (bond lengths and angles, unit cell parameters,) remained consistent with those measured in PXRD experiments. This also prevented any thermal stress from altering the distribution of halide anions in structures. A detailed description of the SCXRD analysis can be found in the **SI**.

SCXRD results on pure-bromide and pure-iodide structures corroborate earlier literature reports.[7,20] They confirm that $(BA)_2MAPb_2Br_7$ and $(BA)_2MAPb_2I_7$ crystallize in the *C*cc2 and *C*cm2$_1$ space groups, respectively (**Figure 3a**). $(BA)_2MAPb_2Br_7$ adopts an octahedral tilting mode, denoted $(00\Phi_z)$ in Aleksandrov notation (**Figure 3b,** top),[21] with pairs of octahedra rotated in antiphase around the *b*-axis by ~10°. $(BA)_2MAPb_2I_7$ adopts a $(\Phi_1\Phi_10)$ tilting mode (**Figure 3b,** bottom), with the two

combined tilts resulting in an antiphase rotation of octahedra around the *c*-axis (8.6°). In contrast, the x = 0.5 $(BA)_2MAPb_2(Br_{0.5}I_{0.5})_7$ specimen crystallizes in the higher symmetry space group *F*mmm (**Figure 3a**, middle). Consistent with assumptions in our geometric model, the transition between these two incompatible tilting modes suppresses any tilt (**Figure 3b,** middle), a condition denoted (000). This conclusively demonstrates that a coexistence of I^- and Br^- in 2D RP structures can cause major modifications to their crystal symmetry.

Crucially, a bond length analysis of the x_{tot} = 0.5 $(BA)_2MAPb_2(Br_{0.5}I_{0.5})_7$ sample indicates that Ap positions are mostly occupied by iodine (Ap = 29% Br, 71% I). Eq positions are instead richer in bromine (Eq = 74% Br, 26% I) while Ct positions are occupied more homogeneously (Ct = 42% Br, 58% I), corresponding to a crystal composition of x_{tot} = 0.56 (**Table S5**). Those results are very close to the halide distribution predicted by the geometric model for x = 0.5. A complementary analysis of halide site occupation via electron densities confirms the same trend and suggests a more marked preference of Apical and Central sites for Iodine (Ap = 7% Br, 93% I; Ct = 37% Br, 63% I; Eq = 64% Br, 36% I). The extracted crystal composition is x_{tot} = 0.44, again compatible within error with the target x_{tot} = 0.5 composition (**Table S6**).

Overall, both PXRD and SCXRD data point to a preferential positioning of I^- and Br^- anions in lead-based mixed-halide RP structures. Discrepancies in determined occupancies likely stem from a combination of model assumptions (e.g., $x_{Ct} \approx x_{tot}$), approach biases (bond lengths vs electron density), and crystallization speeds. The last point is especially relevant, given that sample preparation methods might influence the crystallization dynamics and therefore the distribution of anions within mixed-halide RP structures. However, both PXRD and SCXRD showed clear evidence of preferential halide positioning, and were crystallized over minutes and hours, respectively. Therefore, the question arises whether *faster* crystallization conditions might favor a more homogeneous halide distribution. To address this question, we have collected XRD patterns of n = 2 $(BA)_2MAPb_2(Br_xI_{1-x})_7$ and n = 1 $(BA)_2Pb_2(Br_xI_{1-x})_4$ RP perovskites thin films prepared by spin coating (**Figures S6-7)**. The latter

$n = 1$ specimens are of particular interest given extensive prior investigations of these materials.[8,9,12,13] Details of the thin film spin coating synthesis have been provided in the **SI**.

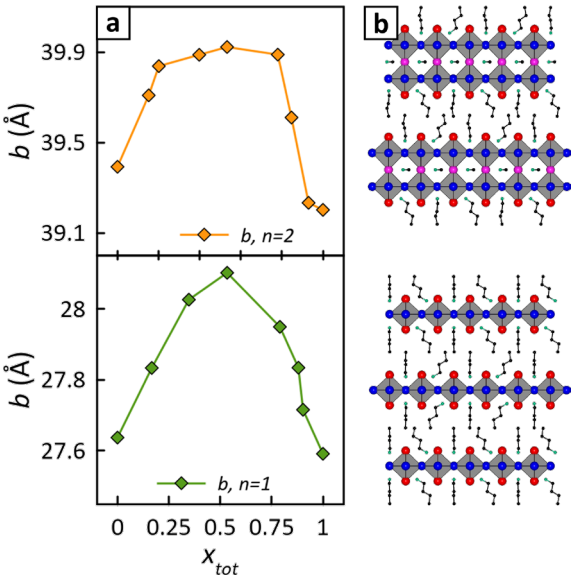

Figure 4. Cell parameter *b* in thin films. a) Experimental *b* parameter measured on $n = 2$ (top) and $n = 1$ (bottom) thin films prepared by spin coating. b) Structure schemes of $n = 2$ $(BA)_2MAPb_2X_7$ (top) and $n = 1$ $(BA)_2PbX_4$ (bottom) RP perovskites.

For both $n = 1$ and $n = 2$ thin films, **Figure 4** shows clear non-linear *b* dependencies with halide composition. This confirms that halide sites in mixed-halide RP perovskites are preferentially occupied even under the fast crystallization conditions often adopted for fabricating samples and devices.[1–3,9,12–14,22] Notably, both $n = 1$ and $n = 2$ samples demonstrate comparable maximum expansion along *b* ($n = 1$: +1.58%; $n = 2$: +1.73%).

To conclude, the common assumption that anions in mixed-halide perovskites are homogeneously distributed at the unit cell level, that holds for 3D perovskites because their halide sites share comparable chemical environments,[15,16,23–25] does not apply to RP layered perovskites. In RP perovskites, instead, I^- anions preferentially occupy Apical sites that are closest to long chain organic cations, while Br^- anions prefer to reside in Equatorial sites, surrounded by lead cations. This preferential positioning occurs regardless of the crystallization speed, and is likely due to the different ionic radii of iodine and bromine. Our conclusions are supported by recent reports on lead-based

mixed-halide RP perovskites[9,17,26] and appear to be part of a broader trend that extends beyond the domain of lead-based materials, wherein structural anisotropy emerges to inhibit halide alloying.[17–19,27,28]

Although the impact of such inhomogeneous halide distribution on the optoelectronic properties of mixed-halide RP perovskites has yet to be fully investigated, there are reasons to believe that it might not be negligible. Indeed, we demonstrated that mixed-halide RP samples can adopt altered symmetry and octahedral tilting modes compared to pure-halide RP specimens. This might affect the orbital overlap, and thus the electronic structure of these materials. Moreover, being aware of preferential anion occupation in mixed-halide RP structures might assist in better understanding the recent observations of anion photo-segregation in these materials.

Supporting Information

Synthesis and characterization methods; oriented- and powder-XRD patterns of $(BA)_2MAPb_2(Br_xI_{1-x})_7$ polycrystalline samples, and Le Bail fits of the latter; outline of the RP structure geometric model; discussion of SCXRD analyses; additional characterization of spin coated thin films. (PDF)

Crystallographic Information Files of the $(BA)_2MAPb_2Br_7$ structure solved by SCXRD (CIF)

Crystallographic Information Files of the $(BA)_2MAPb_2I_7$ structure solved by SCXRD (CIF)

Crystallographic Information Files of the $(BA)_2MAPb_2(Br_xI_{1-x})_7$ structure solved by SCXRD (CIF)

Acknowledgements

MK thanks the Division of Materials Sciences and Engineering, Office of Basic Energy Sciences, U.S. Department of Energy (DOE) under Award DE-SC0014334 for financial support of this work.

MK and VT also thank the NSF for partial financial support under award DMR-1952841. We thank Adam Jaffe, Vadim Trepalin, Jeff DuBose and Preethi Mathews for helpful discussions.

ORCID

Stefano Toso: 0000-0002-1621-5888

Irina Gushchina: 0000-0001-6930-2101

Allen Oliver: 0000-0002-0511-1127

Liberato Manna: 0000-0003-4386-7985

Masaru Kuno: 0000-0003-4210-8514

References

1. Li, X., Hoffman, J. M. & Kanatzidis, M. G. The 2D Halide Perovskite Rulebook: How the Spacer Influences Everything from the Structure to Optoelectronic Device Efficiency. *Chem. Rev.* **121**, 2230–2291 (2021).

2. Tsai, H. *et al.* High-Efficiency Two-Dimensional Ruddlesden-Popper Perovskite Solar Cells. *Nature* **536**, 312–317 (2016).

3. Smith, I. C., Hoke, E. T., Solis-Ibarra, D., McGehee, M. D. & Karunadasa, H. I. A Layered Hybrid Perovskite Solar-Cell Absorber with Enhanced Moisture Stability. *Angew. Chemie - Int. Ed.* **53**, 11232–11235 (2014).

4. Grancini, G. *et al.* One-Year Stable Perovskite Solar Cells by 2D/3D Interface Engineering. *Nat. Commun.* **8**, 1–8 (2017).

5. Liu, Y. *et al.* Surface-Tension-Controlled Crystallization for High-Quality 2D Perovskite Single Crystals for Ultrahigh Photodetection. *Matter* **1**, 465–480 (2019).

6. Dhanabalan, B. *et al.* Engineering the Optical Emission and Robustness of Metal-Halide Layered Perovskites through Ligand Accommodation. *Adv. Mater.* **33**, 2008004 (2021).

7. Stoumpos, C. C. *et al.* Ruddlesden-Popper Hybrid Lead Iodide Perovskite 2D Homologous Semiconductors. *Chem. Mater.* **28**, 2852–2867 (2016).

8. Wright, N. E. *et al.* Influence of Annealing and Composition on the Crystal Structure of Mixed-Halide, Ruddlesden-Popper Perovskites. *Chem. Mater.* **34**, 3109–3122 (2022).

9. Ovčar, J. *et al.* Mixed Halide Ordering as a Tool for the Stabilization of Ruddlesden-Popper Structures. *Chem. Mater.* **34**, 4286–4297 (2022).

10. Pan, D. *et al.* Deterministic Fabrication of Arbitrary Vertical Heterostructures of Two-Dimensional Ruddlesden–Popper Halide Perovskites. *Nat. Nanotechnol.* **16**, 159–165 (2021).

11. Roy, C. R. *et al.* Anion Exchange of Ruddlesden-Popper Lead Halide Perovskites Produces Stable Lateral Heterostructures. *J. Am. Chem. Soc.* **143**, 5212–5221 (2021).

12. Mathew, P. S., Dubose, J. T., Cho, J. & Kamat, P. V. Spacer Cations Dictate Photoinduced Phase Segregation in 2D Mixed Halide Perovskites. *ACS Energy Lett.* **6**, 2499–2501 (2021).

13. Cho, J., Mathew, P. S., DuBose, J. T. & Kamat, P. V. Photoinduced Halide Segregation in Ruddlesden–Popper 2D Mixed Halide Perovskite Films. *Adv. Mater.* **33**, 2105585 (2021).

14. Liu, Y. *et al.* Photoinduced iodide repulsion and halides-demixing in layered perovskites. *Mater. Today Nano* **18**, 100197 (2022).

15. Brivio, F., Caetano, C. & Walsh, A. Thermodynamic Origin of Photoinstability in the $CH_3NH_3Pb(I_{1-x}Br_x)_3$ Hybrid Halide Perovskite Alloy. *J. Phys. Chem. Lett.* **7**, 1083–1087 (2016).

16. Frost, J. M. *et al.* Atomistic Origins of High-Performance in Hybrid Halide Perovskite Solar Cells. *Nano Lett.* **14**, 2584–2590 (2014).

17. Kubo, H. Distribution of Cl- and Br- Ions in Mixed Crystals $(CH_3NH_3)_2Cu(Cl_{1-x}Br_x)_4$. *J. Phys. Soc. Japan* **52**, 1420–1426 (1983).

18. Martinelli, A., Ray, A., Abdelhady, A. L. & Locardi, F. Structural properties of defective $(CH_3NH_3)_2Cu(Cl_{1-x}Br_x)_4$ compounds. *Acta Crystallogr. B. Struct. Sci. Cryst. Eng. Mater.* **78**, 425–435 (2022).

19. Ray, A. *et al.* Impact of local structure on halogen ion migration in layered methylammonium copper halide memory devices. *J. Mater. Chem. A* **8**, 17516–17526 (2020).

20. Liang, M. *et al.* Free Carriers versus Self-Trapped Excitons at Different Facets of Ruddlesden-Popper Two-Dimensional Lead Halide Perovskite Single Crystals. *J. Phys.*

Chem. Lett. **12**, 4965–4971 (2021).

21. Aleksandrov, K. S. & Bartolome, J. Octahedral tilt phases in perovskite-like crystals with slabs containing an even number of octahedral layers. *J. Phys. Condens. Matter* **6**, 8219–8235 (1994).

22. Cao, D. H., Stoumpos, C. C., Farha, O. K., Hupp, J. T. & Kanatzidis, M. G. 2D Homologous Perovskites as Light-Absorbing Materials for Solar Cell Applications. *J. Am. Chem. Soc.* **137**, 7843–7850 (2015).

23. Jong, U. G., Yu, C. J., Ri, J. S., Kim, N. H. & Ri, G. C. Influence of halide composition on the structural, electronic, and optical properties of mixed $CH_3NH_3Pb(I_{1-x}Br_x)_3$ perovskites calculated using the virtual crystal approximation method. *Phys. Rev. B* **94**, 125139 (2016).

24. Beal, R. E. *et al.* Cesium Lead Halide Perovskites with Improved Stability for Tandem Solar Cells. *J. Phys. Chem. Lett.* **7**, 746–751 (2016).

25. Lehmann, F. *et al.* The phase diagram of a mixed halide (Br, I) hybrid perovskite obtained by synchrotron X-ray diffraction. *RSC Adv.* **9**, 11151–11159 (2019).

26. Li, J. *et al.* $Cs_2PbI_2Cl_2$, All-Inorganic Two-Dimensional Ruddlesden-Popper Mixed Halide Perovskite with Optoelectronic Response. *J. Am. Chem. Soc.* **140**, 11085–11090 (2018).

27. Cortecchia, D. *et al.* Lead-Free $MA_2CuCl_xBr_{4-x}$ Hybrid Perovskites. *Inorg. Chem.* **55**, 1044–1052 (2016).

28. Chen, H. P. *et al.* Tunable dielectric transitions in layered organic–inorganic hybrid perovskite-type compounds: $[NH_3(CH_2)_2Cl]_2[CdCl_{4-4x}Br_{4x}]$ (x = 0, 1/4, 1). *Dalt. Trans.* **47**, 7005–7012 (2018).

Supporting Information for

Are Mixed-Halide Ruddlesden-Popper Perovskites Really Mixed?

Stefano Toso[1,2,3,], Irina Gushchina[1], Allen G. Oliver[1], Liberato Manna[3], Masaru Kuno[1,4]*

1) Department of Chemistry and Biochemistry, University of Notre Dame, Notre Dame, IN 46556, USA
2) International Doctoral Program in Science, Università Cattolica del Sacro Cuore, 25121 Brescia, Italy
3) Department of Nanochemistry, Istituto Italiano di Tecnologia, Via Morego 30, 16163 Genova, Italy
4) Department of Physics, University of Notre Dame, Notre Dame, IN 46556, USA

E-mail: stefano.toso@iit.it

Methods

Chemicals

Lead bromide ($PbBr_2$, >98% trace metal basis), lead iodide (PbI_2, 99.999% trace metal basis), methylammonium bromide [CH_6NBr (MABr), 98%], methylammonium iodide [CH_6NI (MAI), 98%], butylammonium bromide [$C_4H_{12}NBr$ (BABr), 98%], butylammonium iodide [$C_4H_{12}NI$ (BAI), 98%], hydrobromic acid (HBr, 48% aq.), hydroiodic acid (HI, 57% aq.), and hypophosphorous acid (H_3PO_2, 99% aq.) were purchased from Sigma-Aldrich. All chemicals were used without further purification.

Synthesis of $(BA)_2MAPb_2X_7$ samples

In brief, MABr, MAI, BABr, BAI, $PbBr_2$ and PbI_2 were weighed inside 8 mL glass vials (MA = methylammonium, BA = butylammonium). To this, known amounts of concentrated aqueous solutions of HBr, HI and H_3PO_2 were added. **Table S1** provides specific amounts of each reagent used.

Table S1. Stock solution compositions for $(BA)_2MAPb_2(Br_xI_{1-x})_7$ samples.

Feed Ratio (x_{feed})	Final Composition (x_{tot})	BABr (g)	BAI (g)	MABr (g)	MAI (g)	$PbBr_2$ (g)	PbI_2 (g)	HBr (mL)	HI (mL)	H_3PO_2 (mL)
0	**0**	---	0.173	---	0.099	---	0.544	---	1.818	0.182
0.2	**0.034**	0.026	0.138	0.014	0.079	0.087	0.435	0.321	1.497	0.182
0.4	**0.046**	0.053	0.104	0.028	0.059	0.173	0.326	0.661	1.157	0.182
0.5	**0.079**	0.066	0.086	0.035	0.049	0.217	0.272	0.839	0.979	0.182
0.6	**0.128**	0.079	0.069	0.042	0.039	0.260	0.218	1.023	0.795	0.182
0.7	**0.230**	0.093	0.052	0.049	0.030	0.303	0.163	1.212	0.606	0.182
0.8	**0.489**	0.106	0.035	0.056	0.020	0.346	0.109	1.408	0.410	0.182
0.90	**0.756**	0.119	0.017	0.062	0.010	0.390	0.054	1.610	0.209	0.182
0.95	**0.867**	0.126	0.009	0.066	0.005	0.411	0.027	1.713	0.105	0.182
1.0	**1**	0.132	---	0.069	---	0.433	---	1.818	---	0.182

Powders: Vials were sealed and heated to 130 °C on a hotplate until their contents became limpid light-yellow solutions. Gentle shaking was used to speed up this process. Once solutions turned clear, vials were transferred to a thermostatic water bath, maintained at temperatures between 35-40 °C. Crystalline RP precipitates were obtained within a few minutes of immersion. Gentle shaking was used to speed up this process.

Crystals on substrates: To synthesize RP crystals on substrates, 50 µL of warm (mother liquor) solutions were drop cast onto flat glass or silicon substrates. Crystal nucleation was triggered on cooling and was observed through the formation of yellow-to-orange colored films. Crystal growth was halted by gently pressing paper tissues onto substrates to wick up any excess mother liquor.

PXRD specimens. To retrieve powders for PXRD analyses, vials were cooled to room temperature and were centrifuged to compact powders onto their bottoms (2500 rpm, 5 minutes). Any supernatant was removed using a pipette. Wet solids were then recovered with a spatula and deposited onto filter paper. Samples were dried through gentle pressing with additional filter paper. Recovered solids were then transferred to a mortar and were gently ground with a pestle to randomize the orientation of RP crystallites. Powders were finally transferred into a cylindric sample holder (~6 mm diameter ×3 mm depth) and were gently pressed to obtain flat pellets for PXRD analysis.

SCXRD samples. Single crystal specimens were prepared in a manner similar to that of powder samples. The main difference was that samples were cooled from 130 °C to room temperature with a controlled temperature descent of -2 °C per hour, using a programmable oven. Additionally, 40 mL vials were used to ease the manipulation of resulting single crystals. Produced specimens contained compact masses of mm-sized crystals, that were highly defective. Consequently, for SCXRD analyses thin shards of approximately 95 mm in lateral size were selected, based on the quality of their polarized light extinction.

Spin-coated films. Pure iodide and bromide precursor solutions were prepared from pure iodide and bromide RP perovskite powder samples, obtained as described above for PXRD specimens. The composition of n = 2 stock solutions is indicated in **Table S1**, while that for n = 1 samples follows: $(BA)_2PbBr_4$ = 0.349 g $PbBr_2$ + 0.085 g BABr + 1.818 ml HBr + 0.182 ml H_3PO_2; $(BA)_2PbI_4$ = 0.438 g PbI_2 + 0.111 g BAI + 1.818 ml HI + 0.182 ml H_3PO_2. The as-prepared RP perovskite powders were weighed and dissolved in anhydrous dimethylformamide (DMF), using suitable volumes to produce equimolar solutions of n = 1 $(BA)_2PbBr_4$ and $(BA)_2PbI_4$ and n = 2 $(BA)_2MAPb_2Br_7$ and $(BA)_2MAPb_2I_7$. To obtain mixed-halide $(BA)_2PbX_4$ and $(BA)_2MAPb_2X_7$ thin film specimens, precursor solutions were pre-mixed in the desired stoichiometric ratio and coated onto plasma-treated glass coverslips.

Characterization

EDXS analysis. Compositional analysis was performed on a Thermo Prisma Environmental-SEM equipped with an EDXS probe. Crystalline samples were deposited onto silicon substrates and were measured without additional sputtering of conductive coatings. Compositional data were acquired in mapping mode on regions of interest, comparable in size with microcrystal (010) facets. Multiple microcrystals (N~5) were analyzed for each RP composition made. Average stoichiometries are provided in **Figure S1**. Spin coated film samples were analyzed in 3 different regions of the film to average the compositional analysis.

PXRD and Le Bail analysis. Powder XRD patterns were collected on a Bruker D8 Advance diffractometer, equipped with a Cu Kα source and a LynxEye pixel detector operating in a Bragg-Brentano geometry in reflection mode. PXRD patterns were analyzed by performing Le Bail fits using the program Profex.[1] Prior to analysis, manual background subtraction was performed to improve fit convergence. The Le Bail analysis does not assume any structural constraints on the intensities of diffraction peaks. Hence, it is ideal for refining unit cell parameters, but does not provide any structural information beyond this.

SCXRD analysis. SCXRD data were collected on a Bruker Apex II single-crystal diffractometer, equipped with a Mo-Kα source and Apex-II detector. Data were collected at room temperature using Apex-4 software. Subsequent data analysis and structure solution were performed using the software suite Olex2.[2] Details of the refinements are provided in the "*Single-crystal X-ray diffraction results*" section below.

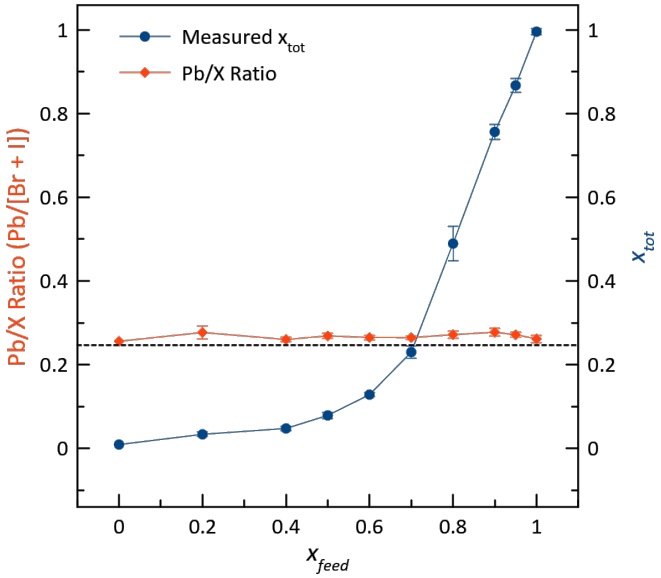

Figure S1. Composition calibration curve for $(BA)_2MAPb_2(Br_xI_{1-x})_7$ crystals. Blue trace: experimental halide composition plotted versus halide precursor feed ratio. Red trace: experimental Pb/X ratio as measured by SEM-EDXS. In both scales, x = Br/[Br+I] where Br and I are the atomic fractions of bromine and iodine introduced in precursor solutions (feed ratio) and measured experimentally by SEM-EDXS (measured). Solid blue and red lines are guides to the eye. The horizontal, dashed black line represents the ideal Pb/X value of 2/7 = 0.286, established by the stoichiometry of $(BA)_2MAPb_2X_7$. This line serves as a control to assess the reliability of SEM-EDXS analyses.

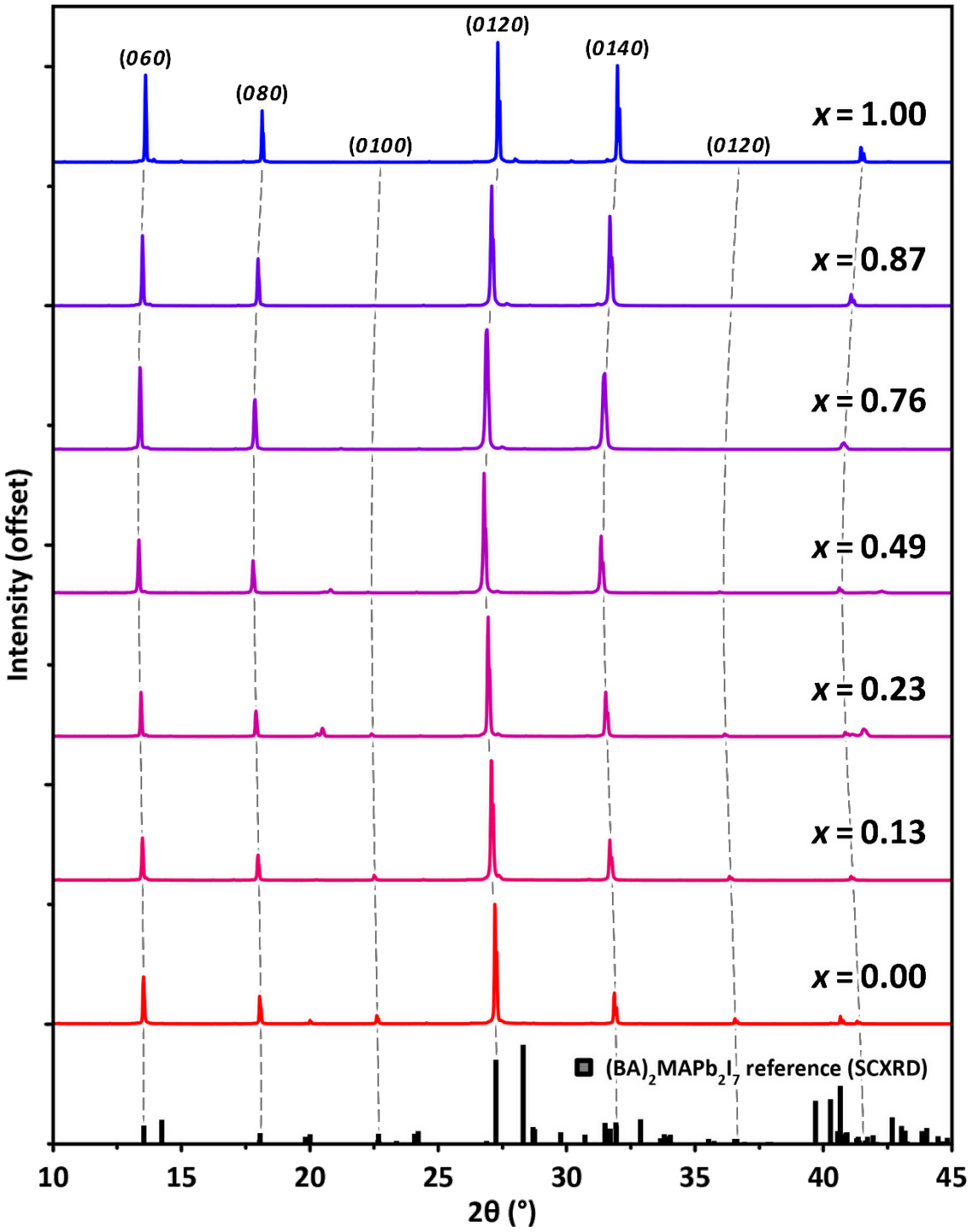

Figure S2. XRD patterns of $(BA)_2MAPb_2(Br_xI_{1-x})_7$ crystals oriented flat on substrates. Data were collected on samples prepared for SEM-EDXS analysis. All patterns show a series of intense and regularly spaced reflections typical of RP perovskite crystals laying with (*02k0*) planes parallel to the substrate. All peaks are captured by the same periodicity, indicating that only the n = 2 $(BA)_2MAPb_2(Br_xI_{1-x})_7$ phase is present, and no contaminant RP phases with n = 1 or n ≥ 3 were formed. The few, weak peaks not belonging to the periodic series come from misoriented crystals of $(BA)_2MAPb_2(Br_xI_{1-x})_7$ RP perovskites, as seen by comparison with the reference pattern (reference structure from this work).

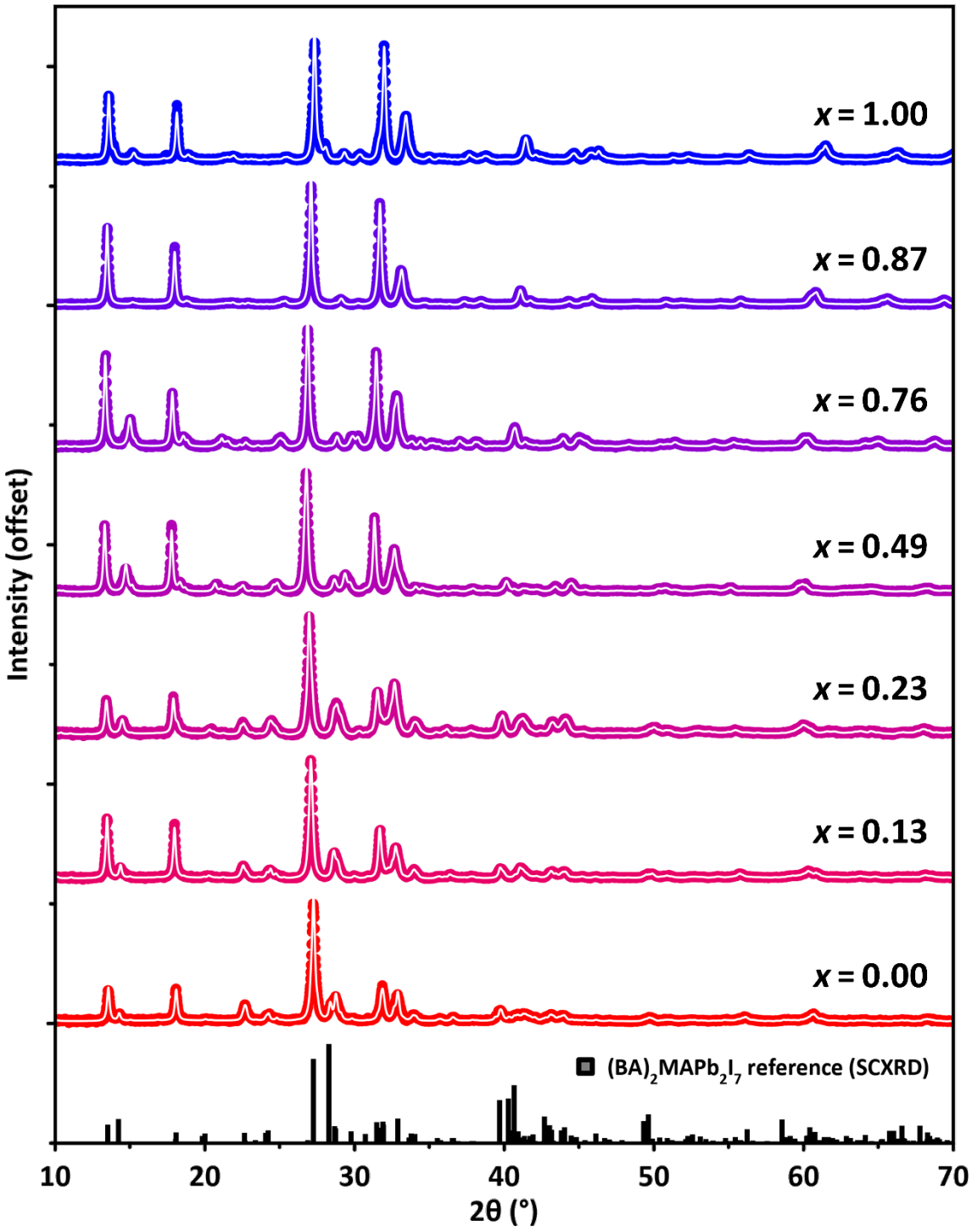

Figure S3. Le Bail fits of $(BA)_2MAPb_2(Br_xI_{1-x})_7$ PXRD patterns. Experimental PXRD patterns collected on $(BA)_2MAPb_2(Br_xI_{1-x})_7$ samples (colored markers) with Le Bail fit profiles superimposed (solid white lines). All peaks in the diffraction patterns could be indexed based on the expected $(BA)_2MAPb_2(Br_xI_{1-x})_7$ structures, indicating that all samples are phase-pure. The reference pattern is calculated based on the $(BA)_2MAPb_2I_7$ RP perovskite structure solved in this work by SCXRD.

RP structure geometric model

As discussed in the main text, RP unit cell parameters can be written as:

$$a^* = \frac{4[\mathrm{Pb{-}X}]_{\mathrm{Eq}} \sin\frac{\beta}{2}}{\sqrt{2}} \quad \textbf{(S1)}$$

$$b = 2L + 4[\mathrm{Pb-X}]_{\mathrm{Ct}} \sin\frac{\alpha}{2} \quad \textbf{(S2)}$$

Where [Pb-X] is the Pb-X bond length, with subscripts indicating the relative halide site, L is the Pb-Pb vertical distance between neighboring $[PbX_6]^{4-}$ octahedra layers, α is the Pb-X-Pb bond angle between vertically stacked $[PbX_6]^{4-}$ octahedra, and β is the X-Pb-X bond angle between neighboring $[PbX_6]^{4-}$ octahedra in the equatorial plane (see **Figure S4a**). The meaning and derivation of each term is discussed below.

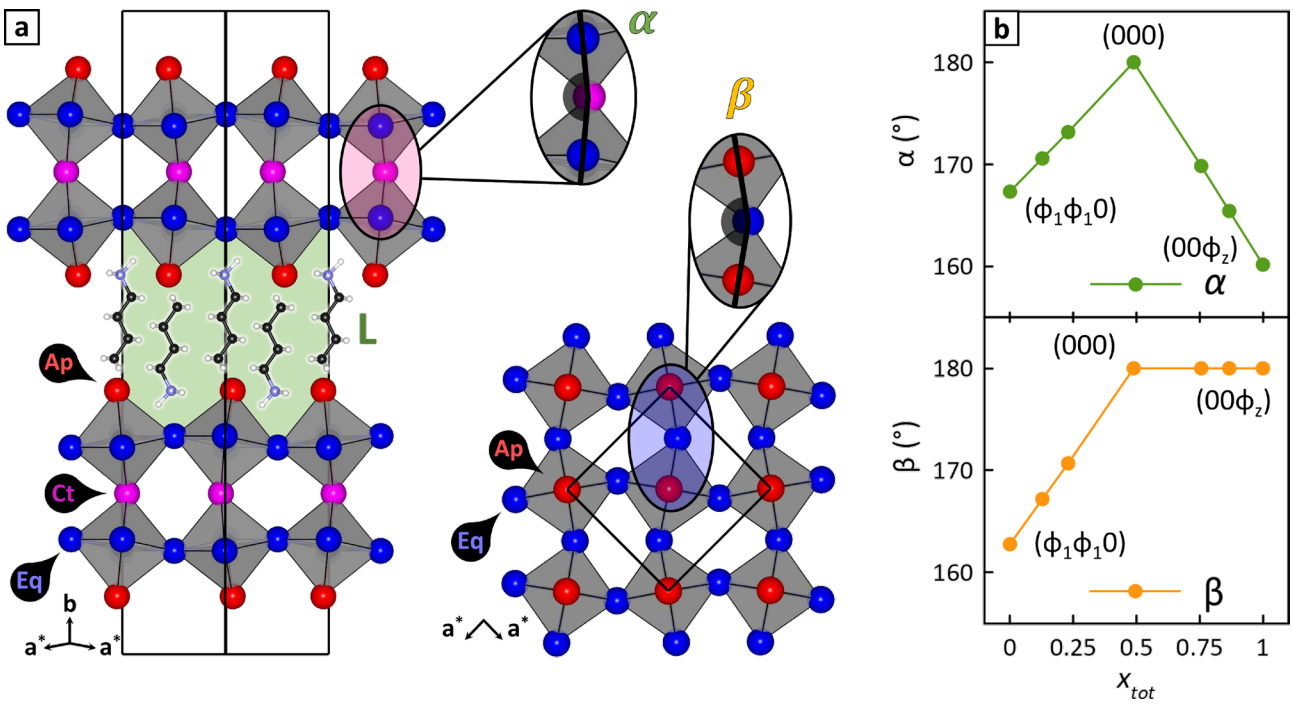

Figure S4. RP structure geometric model. a) Two different views of the RP unit cell, highlighting key features of the model. Apical, Equatorial and Central sites are indicated by black labels (Ap, Eq, and Ct). The interlayer distance, L, is shown in green. Insets show the α and β bond angles. b) Modeled dependence of α and β on x_{tot}. Aleksandrov notation shown for the transition structure at $x_{tot} = 0.5$ and for corresponding pure-halide limiting structures.

1) Fractional composition of halide X sites in the RP unit cell.

Bilayer RP structures feature three different kinds of halide (X) sites: Apical (Ap), Equatorial (Eq) and Central (Ct). The total number of X sites per formula unit is 7, as indicated by the stoichiometry $(BA)_2MAPb_2X_7$. Of these, 2 are Apical, 4 are Equatorial and 1 is Central. **Equation S3** relates the total halide sample composition (x_{tot}), measured by SEM-EDXS, with that of each X site weighted by their multiplicity:

$$x_{\mathrm{tot}} = \frac{2}{7}x_{\mathrm{Ap}} + \frac{4}{7}x_{\mathrm{Eq}} + \frac{1}{7}x_{\mathrm{Ct}}. \quad \textbf{(S3)}$$

Central sites closely resemble those found in 3D-$APbX_3$ perovskites, and hence are most likely to be occupied by I^- and Br^- with little or no preference. It is therefore assumed that $x_{\mathrm{Ct}} \approx x_{\mathrm{tot}}$.

2) [Pb-X] bond lengths as functions of X site composition.

[Pb-X] bond lengths are linear combinations of [Pb-Br] and [Pb-I] bond lengths, weighted by the composition of respective halide sites:

$$[\mathrm{Pb-X}]_{\mathrm{Eq}} = x_{\mathrm{Eq}}[\mathrm{Pb-Br}]_{\mathrm{Eq}} + (1 - x_{\mathrm{Eq}})[\mathrm{Pb-I}]_{\mathrm{Eq}} \quad \textbf{(S4)}$$

$$[\mathrm{Pb-X}]_{\mathrm{Ap}} = x_{\mathrm{Ap}}[\mathrm{Pb-Br}]_{\mathrm{Ap}} + (1 - x_{\mathrm{Eq}})[\mathrm{Pb-I}]_{\mathrm{Ap}} \quad \textbf{(S5)}$$

$$[\mathrm{Pb-X}]_{\mathrm{Ct}} = x_{\mathrm{Ct}}[\mathrm{Pb-Br}]_{\mathrm{Ct}} + (1 - x_{\mathrm{Ct}})[\mathrm{Pb-I}]_{\mathrm{Ct}} \quad \textbf{(S6)}$$

Table S2 provides SCXRD-measured values for [Pb-Br] and [Pb-I] bond lengths in pure-halide $(BA)_2MAPb_2Br_7$ and $(BA)_2MAPb_2I_7$.

Table S2. SCXRD [Pb-Br] and [Pb-I] bond lengths.

SCXRD Data	[Pb-Br]	[Pb-I]
Ap	2.914 Å*	3.083 Å
Eq**	2.992 Å	3.173 Å
Ct	3.064 Å	3.267 Å

* *$[Pb\text{-}Br]_{Ap}$ is calculated between Pb and the average position of two disordered Br sites, see (BA)2MAPb2I7.cif*

** *$[Pb\text{-}X]_{Eq}$ values are the average of the four equatorial bond lengths*

3) Bond angles α and β

The bond angles α and β depend on the octahedra tilting mode adopted by the RP structure. The two pure-halide compounds, $(BA)_2MAPb_2Br_7$ and $(BA)_2MAPb_2Br_7$, exhibit different tilting modes [$(00\Phi_z)$ and $(\Phi_1\Phi_10)$, respectively]. It is assumed that x_{tot} = 0.5 represents a sharp transition between these tilting modes, with x_{tot} = 0.5 adopting a no-tilting (000) structure.

Angles α and β are therefore assumed to vary linearly within the intervals $0 \leq x_{tot} < 0.5$ and $0.5 \leq x_{tot} \leq 1$, and can be expressed as the following weighted sums (**Equations S7-S8**). **Figure S4b** shows resulting α and β values as x_{tot} increases from 0 to 1.

$$\alpha = f\alpha_{\mathrm{I}} + (1-f)\alpha_{x=0.5} \qquad (x<0.5) \qquad \textbf{(S7a)}$$

$$= (1-f)\alpha_{x=0.5} + f\alpha_{\mathrm{Br}} \qquad (x\geq 0.5) \qquad \textbf{(S7b)}$$

$$\beta = f\beta_{\mathrm{I}} + (1-f)\beta_{x=0.5} \qquad (x<0.5) \qquad \textbf{(S8a)}$$

$$= (1-f)\beta_{x=0.5} + f\beta_{\mathrm{Br}} \qquad (x\geq 0.5) \qquad \textbf{(S8b)}$$

$$f = \frac{0.5-x_{\mathrm{tot}}}{0.5} \qquad \textbf{(S9)}$$

Equation S9 describes f as the Br fraction in the sample, compared to the tilting mode transition value of x_{tot} = 0.5. Limiting α and β values for $(BA)_2MAPb_2Br_7$ and $(BA)_2MAPb_2I_7$ have been measured by SCXRD and are reported in **Table S3**.

Table S3. α and β values for $(BA)_2MAPb_2Br_7$ and $(BA)_2MAPb_2I_7$

Angle	$(BA)_2MAPb_2Br_7$	$(BA)_2MAPb_2I_7$
α	160.2°	167.3°
β	180.0°	162.8°

4) Estimation of L as a function of a^* and x_{Ap}

The distance L between two neighboring $[PbX_6]^{4-}$ bilayers, measured at the Pb^{2+} ion plane level, is established as follows. The space between bilayers is considered occupied by neutral L-X ligands, whose volume $V_{L\text{-}X} = V_L + V_X$ is the sum of the constant ammonium chain volume V_L and the variable halide volume V_X. Overall, the $V_{L\text{-}X}$ volume is assumed to be a weighted sum of limiting BA-I and BA-Br volumes ($V_{L\text{-}Br}$ and $V_{L\text{-}I}$ respectively):

$$V_{\mathrm{L}} = x_{\mathrm{Ap}}V_{\mathrm{L-Br}} + (1-x_{\mathrm{Ap}})V_{\mathrm{L-I}}. \qquad \textbf{(S10)}$$

Since the volume occupied by L-X ligands is confined vertically by octahedra layers and horizontally by unit cell faces, it can be calculated as:

$$V_{\mathrm{L-X}} = \frac{(a^*)^2 L}{4}. \quad \textbf{(S11)}$$

Where the ¼ factor is due to the presence of four L-X units per $(a^*)^2$ unit area. Terminal $V_{\mathrm{L\text{-}Br}}$ and $V_{\mathrm{L\text{-}I}}$ values are calculated based on SCXRD-determined a^* parameters and L lengths, and are reported in **Table S4**.

Table S4. SCXRD V_{L} values for $(BA)_2MAPb_2Br_7$ and $(BA)_2MAPb_2I_7$

$V_{\mathrm{L\text{-}Br}}$	$V_{\mathrm{L\text{-}I}}$
234.3 Å^3	261.4 Å^3

Finally, **Equation S11** can be inverted to yield L as a function of a^* (**Equation S12**). This relation can be used to calculate L for mixed-halide samples. Note that L is a function of x_{Ap} through the term $V_{\mathrm{L\text{-}X}}$ as well as a function of x_{Eq} through the term a^*.

$$L = 4 \cdot \frac{V_{\mathrm{L-X}}}{(a^*)^2} \quad \textbf{(S12)}$$

To validate the assumption that $V_{\mathrm{L}} \approx$ constant and $V_{\mathrm{L\text{-}X}}$ only depends on the composition of the Apical site, we compared the volume variation induced by the Br→I replacement in one unit of BA-X (our samples, **Table S4**) and in one unit of NH_4X (published NH_4X structures, NH_4Br = 66.9 Å^3 [ICSD-24916]; NH_4I = 95.7 Å^3 [ICSD-22150]). Replacing Br→I in NH_4X results in ΔV = 28.8 Å^3, that is very close to $\Delta V = V_{\mathrm{L\text{-}I}} - V_{\mathrm{L\text{-}Br}}$ = 27.1 Å^3 measured for our samples. This demonstrates that the volume variation can be entirely attributed to the halide replacement and, therefore, that the volume occupied by ammonium cations remains unchanged.

We also compared the $V_{\mathrm{L\text{-}X}}$ values in n = 2 $(BA)_2MAPb_2X_7$ structures (our samples, **Table S4**) and in n = 1 $(BA)_2PbX_4$ structures (published: COD-1545801; COD-2102938). These are remarkably close for both bromine-based ($V_{\mathrm{L\text{-}Br}}$ = 236.6 Å^3 [n=1] vs 234.4 Å^3 [n=2]) and iodine-based compounds ($V_{\mathrm{L\text{-}I}}$ = 266.2 Å^3 [n=1] vs 261.4 Å^3 [n=2]), even if the compared structures feature drastically different stoichiometries and adopt different octahedra tilting modes. Moreover, for n = 1 structures the Br→I replacement results in ΔV = 29.7 Å^3, again fully compatible with the examples discussed above. This further demonstrates that considering constant the volume V_{L} occupied by ammonium cations is a robust and reliable approximation.

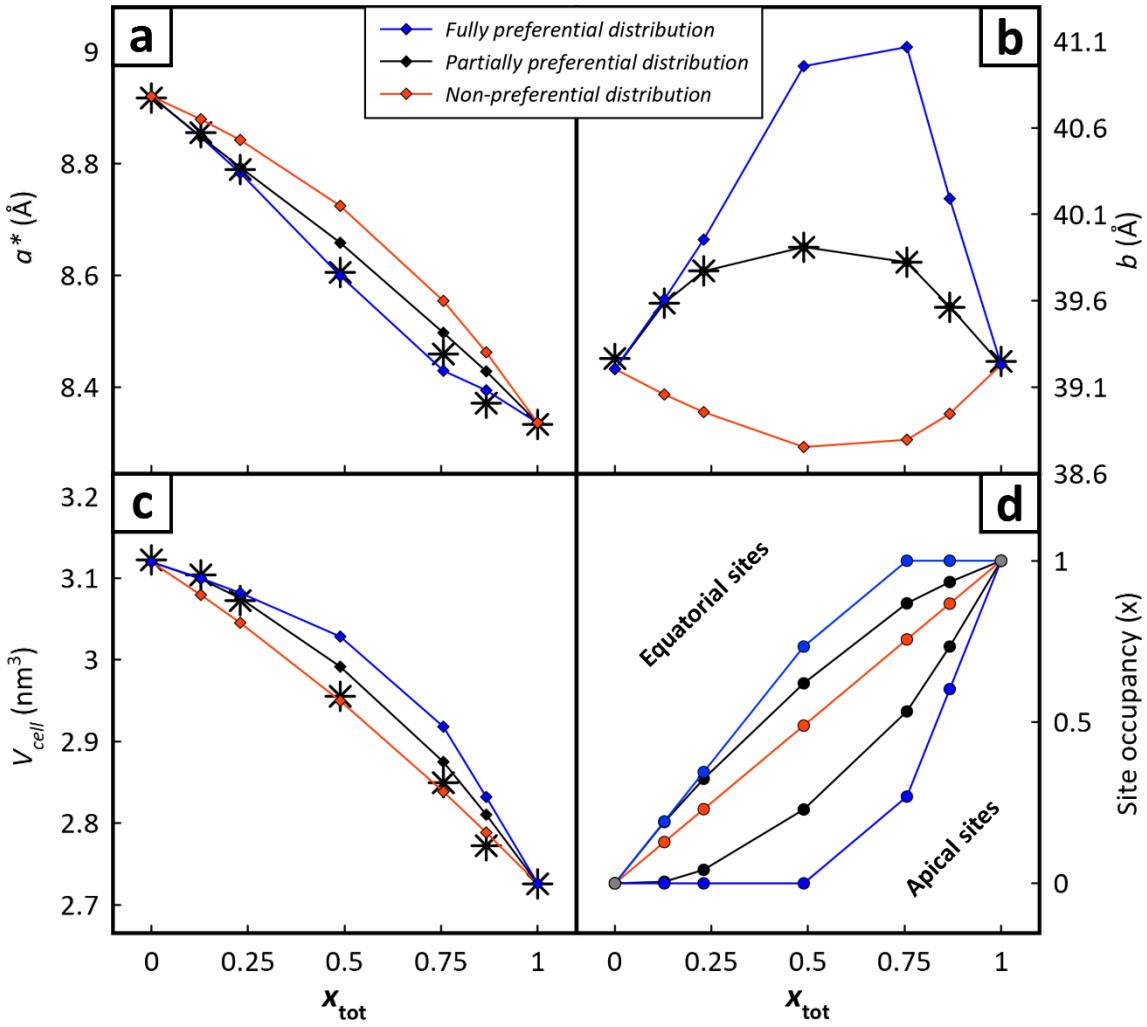

Figure S5. Fully preferential and non-preferential halide distribution limit cases. Simulated lattice parameters a^* (panel a), b (panel b), unit cell volume V (panel c) and fractional halide composition of Apical and Equatorial halide sites (panel d) for two limit cases: fully preferential distribution of halides (blue lines) and non-preferential distribution of halides (red lines). Black lines reproduce the case of a partially preferential distribution of halides, as shown in **Figure 2** of the Main Text. Black asterisks represent parameters measured experimentally.

Single-crystal X-ray diffraction results

The structure models obtained from SCXRD data are provided as .cif files: (BA)2MAPb2I7.cif, (BA)2MAPb2I7.cif, and (BA)2MAPb2(Br0.5I0.5)7.cif for pure bromine, pure iodine, and x = 0.5 mixed bromine/iodine RP perovskites, respectively. Data have been recorded at room temperature to allow direct comparisons with room temperature PXRD data. We observe that cooling RP specimens to cryogenic temperatures results in lattice deformations, occasionally accompanied by fracturing.

In general, structures were solved by dual-space methods, and expanded and refined routinely from difference Fourier maps. Due to disorder of alkyl amines, in all three structures the organic cations have been modeled using isotropic displacement parameters. In contrast, Pb, I, and Br atoms have all been modeled using anisotropic displacement parameters. Hydrogen atoms could not be located or geometrically placed on

disordered MA cations. They have, however, been included in the chemical formula for completeness. Hydrogen atoms bonded to BA cations have been modeled in an idealized geometry. In all studied cases, the BA cations are found to be disordered in the interlayer space. The proposed models best account for the electron density therein.

The structure of $(BA)_2MAPb_2Br_7$ has been refined with a racemic twin component, yielding a 0.548:0.452 domain ratio. $(BA)_2MAPb_2I_7$ has likewise been modeled with a racemic twin component, yielding a 0.51:0.49 twin ratio. In both cases, the presence of an inversion center was contraindicated by attempts to model the structures in centrosymmetric space groups and by the lack of missed inversion symmetry in the asymmetric unit. Mild restraints were applied to the bond distances, angles, and displacement parameters of BA and MA cations in all structures. For the mixed-halide $(BA)_2MAPb_2(Br_xI_{1-x})_7$, halogen positions have been refined with Br^- and I^- occupying the same site. Standard equivalencies to constrain atom positions and displacement parameters were employed.

Site occupancies were refined to account for measured electron densities with Br and I fractions adding up to unity. Site compositions were assumed independent of each other. This yielded an overall halide ratio of $x_{tot} = 0.44$, with anions distributed as follows:

Table S5. Halide composition of Ap, Eq, and Ct sites as determined by electron density.

Site	Br %	I %
Ap	7	93
Eq	64	36
Ct	37	63
Total	44	56

For a better comparison with the developed geometric model, site occupancies have also been estimated based on bond lengths by applying **Equations S4-6**. This yields an overall halide ratio of $x_{tot} = 0.56$, with anions distributed as follows:

Table S6. Halide composition of Ap, Eq, and Ct sites as determined by bond lengths.

Site	Br %	I %
Ap	29	71
Eq	74	26
Ct	42	58
Total	56	44

Spin coated thin films

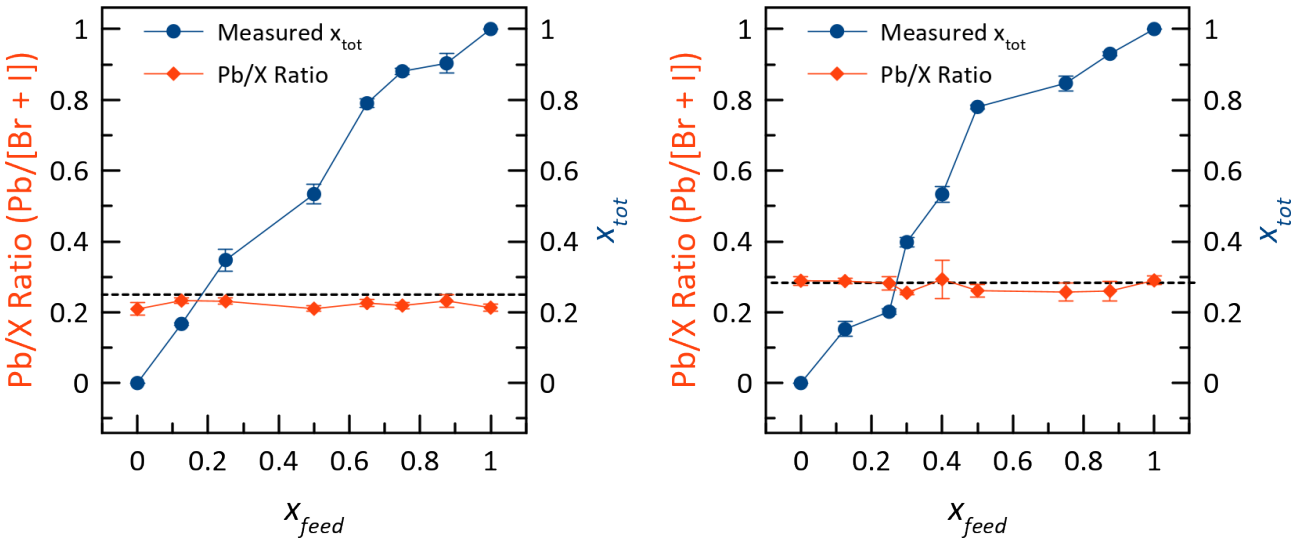

Figure S6. Composition calibration curves for spin coated thin films. a) Calibration curve for $n = 1$ $(BA)_2Pb(Br_xI_{1-x})_4$ films. b) Calibration curve for $n = 2$ $(BA)_2MAPb_2(Br_xI_{1-x})_7$ films. Blue traces: experimental halide composition plotted versus halide precursor feed ratio. Red traces: experimental Pb/X ratio as measured by SEM-EDXS. In both scales, x = Br/[Br+I] where Br and I are the atomic fractions of bromine and iodine introduced in precursor solutions (feed ratio) and measured experimentally by SEM-EDXS (measured). Solid blue and red lines are guides to the eye. Horizontal, dashed black lines represent the ideal Pb/X values of 1/4 = 0.25 for $n = 1$ and 2/7 = 0.286 for $n = 2$, established from the stoichiometry of $(BA)_2MAPb_2X_7$ and $(BA)_2MAPb_2(Br_xI_{1-x})_7$ respectively. These lines serve as controls to assess the reliability of SEM-EDXS analyses.

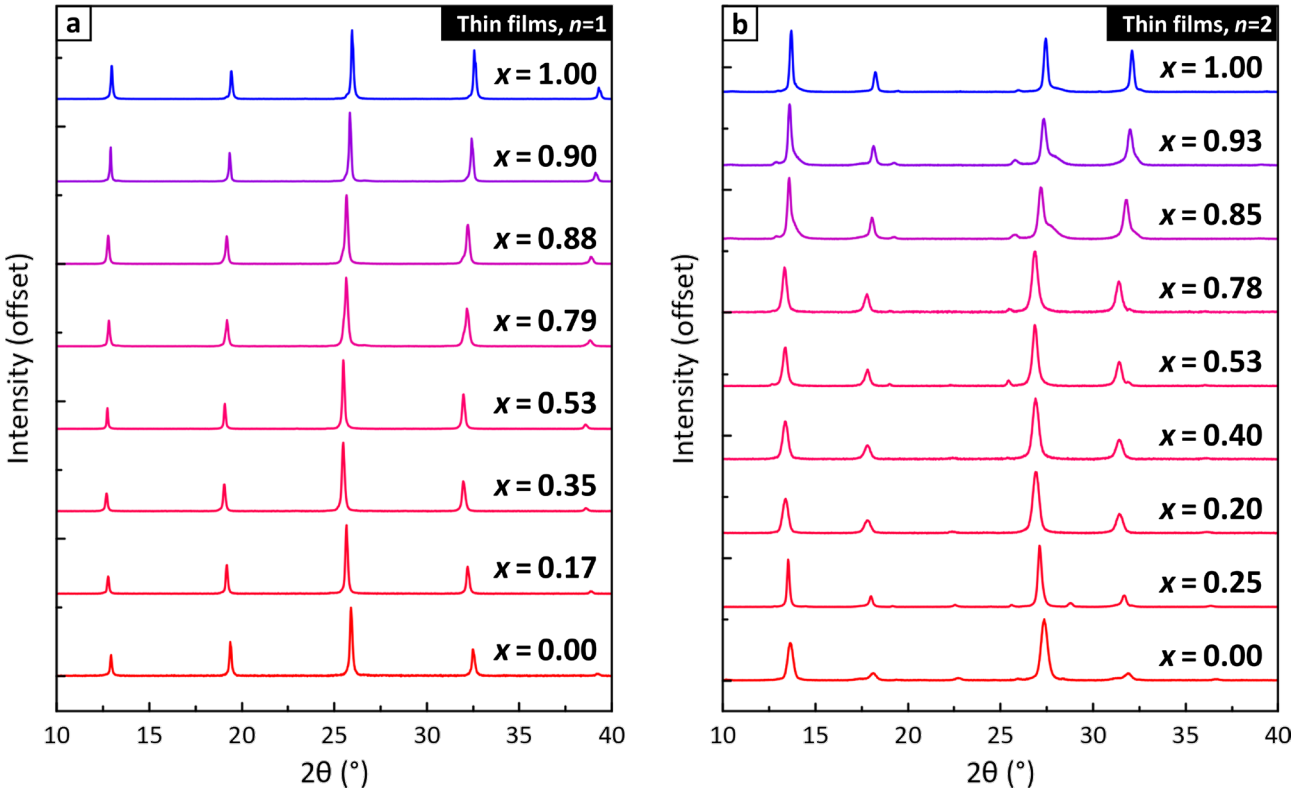

Figure S7. XRD patterns of spin coated thin films. a) $n = 1$ $(BA)_2Pb(Br_xI_{1-x})_4$ and b) $n = 2$ $(BA)_2MAPb_2(Br_xI_{1-x})_7$ films.